Origin of strain tunability in flat valence band and ultrahigh shear piezoelectricity in superflexible non–van der Waals graphitic ScX monolayers (X = P, As, Sb)

Harshita Seksaria, Arneet Kaur, and Abir De Sarkar*
Institute of Nano Science and Technology, Knowledge City, Sector 81, Mohali, Punjab 140306, India

(Received 20 April 2023; revised 6 July 2023; accepted 10 August 2023; published 22 August 2023)

Utilizing the exceptional characteristics of two-dimensional (2D) materials for solid-state electronic devices presents an appealing strategy that could potentially address the need to prolong Moore's law. Evidently, the prevailing fraction of technically viable materials, which have already been successfully scaled up for industrial production, belongs to the category of non–van der Waals (n-vdW) materials. In recent years, research on n-vdW 2D materials has garnered significant growth owing to their potential for diverse applications and the development of synthesis techniques. In this paper, we stabilize 1-atom-thick ScX (X = P, As, Sb) monolayers drawn from their n-vdW bulk counterpart in the wurtzite phase by applying a minimal tensile strain of 1–2%. The resulting high flexibility, owing to the extremely small in-plane elastic constants (6–43 N/m) and Young's modulus (6–20 N/m), suits them ideally for extensive strain engineering on a large scale. Complex mixing of acoustic and optic phonon modes for higher strains ensures a large shear-piezoelectric coefficient of up to $d_{16} = -228.08$, -469.87, and -397.52 pm/V for ScP, ScAs, and ScSb respectively. This coefficient notably surpasses that in amino acids, making it the highest reported to date, and is accompanied by high in-plane piezoelectric coefficients, $|d_{21}|$ and $|d_{22}| > 100$ pm/V and highly strain-tunable shear piezoelectric coefficient d_{15} ranging from -90 to 210 pm/V. The monolayers exhibit rich band structures, including flat bands at the top-most valence band and a large spin splitting of $\sim$100 meV, making them ideal for applications in LED and laser devices and opening exciting avenues for exploration in spintronics. In this paper, we present an in-depth analysis of band flattening caused by tensile strain and demonstrate the strong integrability of ScP monolayer with Si substrate. The ScP monolayer retains its flat band feature when implanted on silicon, which promises significant advancements in various practical applications.

DOI: 10.1103/PhysRevB.108.075426

I. INTRODUCTION

After the introduction of graphene [1], two-dimensional (2D) materials have served as a fertile ground for substantial scientific investigation from both conceptual and practical perspectives. The modern century has already seen several revolutionary material discoveries and technological breakthroughs in 2D materials [2–15], yet the quest for 2D materials remains limited to the ones which have layered three-dimensional (3D) counterparts, that is, the van der Waals (vdW) 2D materials. However, high air sensitivity, difficulty in persistence of performance, and maintenance of desired layer thickness under different temperatures and ambient conditions constrains the use of vdW 2D materials in practical applications. The preponderance of materials currently in use with extensive technological applications includes silicon, metal oxides, nitrides, and sulfides, which are non-vdW (n-vdW) structures, thereby underlining the importance of the latter [16,17].

Due to the difficulties in producing n-vdW materials in the ultrathin limit with substantial lateral size or area, the impact of confinement in one dimension (1D) on these materials is still unexplored. Unlike vdW 2D materials, the synthesis of n-vdW 2D materials has been majorly focused on bottom-up approaches. The interest of the scientific community in this field has recently been rekindled by advances in the cleaving of n-vdW bulk materials by state-of-the-art top-down exfoliation, the liquid phase exfoliation method, to their ultrathin counterparts. This unexpected direction emerged in 2D material research after the successful exfoliation of n-vdW compounds to atomic thin sheets [18,19]. Advancements in synthesis techniques and the development of fabrication methods have enabled the exploration of alternative applications, resulting in the demonstration of cutting-edge device prototypes. After that, many n-vdW 2D materials came into the picture experimentally and theoretically, exhibiting great potential in electronic and optoelectronic properties [20–34], some of which are very crucial from the perspective of practical applications [22,24,25,34].

Moreover, the n-vdW materials consisting of cations with low oxidation states are easier to exfoliate, as shown by their low exfoliation energies, which are even comparable with that in graphene [35]. While exfoliating a n-vdW monolayer from its bulk counterpart, one coordination is reduced, which is to be compensated through a strengthening of the anion-cation bond, i.e., decrease in length of the anion-cation bond. However, the anions with more extended wave functions show inability in doing so. As a result, the binary semiconductors having elements other than the first row do not hold

*abir@inst.ac.in; abirdesarkar@gmail.com

stability at the single-atomic-layer thickness in general [36], e.g., the planar CdS monolayer has been stabilized via minimal biaxial strain. These semiconductors show some unusual features in their band structures. In this paper, we have taken 1-atom-thick hexagonal (h-) ScX (X = P, As, Sb) monolayers, which are dynamically unstable as established in our previous work [21] and another report [37]. The planar graphitic h-ScX monolayers are 2D counterparts of the 3D wurtzite structure of ScX. These monolayers are put through uniform biaxial strain and found to be stabilized with a minor strain of 1–2% and can then withstand strain up to 13–14%. The structural integrity against a high range of strain, coupled with a low elastic constant, results in high flexibility, which in turn provides motivation to engineer material properties using strain.

2D materials have been demonstrated to exhibit superior properties compared with their 3D bulk counterparts in various aspects, among which piezoelectric applications and strain engineering are of our concern for this paper. Piezoelectricity has been studied for various 2D materials [38–43] after a theoretical prediction in 1H-MoS_2 by Duerloo *et al.* [40] followed by its experimental verification [44,45]. High piezoelectric coefficients studied in group-IV(A) [46,47] and group-IV(B) [42] prompted us to explore piezoelectricity in these group-IIIB-VA binary semiconductors. Despite extensive computational investigations into the in-plane and out-of-plane piezoelectricity of 2D materials, there is a relative scarcity of studies focusing on the shear piezoelectricity in these materials. Experimental measurements have shown that the bulk wurtzite GaN and AlN structures have a shear piezoelectric coefficient of 3.1–3.6 $\mathrm{pmV^{-1}}$ [48]. A high piezoelectric shear coefficient d_{15} or d_{16} is needed in various applications such as actuators, sensors, transducers, structural health monitoring, vibration control systems, and pressure sensors [49–54]. Further, shear piezoelectricity is very effective in biomedical applications, considering the helical structures of polymer chains in living bodies [55–58]. Recently, very high shear piezoelectric coefficient d_{15} has been theoretically reported in group-IV(A) Janus dichalcogenide monolayers by Nandi *et al.* [59]. The shear piezoelectric coefficient d_{16} has long been overlooked in scientific research, but a recent article in *Nature Materials* revealed an astonishingly high value of 178 pm/V for β-glycine amino acid [49]. This coefficient has since been used in experimental pressure sensors [50] and biomedical applications [52], sparking interest and potential for this previously underestimated field of study. In this paper, high increase in the shear-mode piezoelectric coefficient (d_{16}) is realized in ScX monolayers accompanied by high in-plane piezoelectric coefficients (d_{21} and d_{22}) through positive tensile strain. Along with that, the shear piezoelectric coefficient d_{15} can be significantly tuned through uniform biaxial tensile strain. Phonon dispersion and electronic structure within this stability range have been studied in detail for ScP, while ScAs and ScSb are expected to show similar behaviors. Complex mixing of optical and acoustic phonon modes supports the high shear-mode piezoelectric coefficient d_{16}.

Another leading field in contemporary physics is the study and development of flat-band materials. Several systems, such as heavy fermions, high-temperature superconducting materials, ^{3}He, and 2D electron systems, are predicted to exhibit a flat band according to theoretical models [60–62]; however, the field was popularized after the realization of nearly flat bands experimentally at the magic angle in twisted bilayer graphene [63]. As the interaction between fermions becomes stronger, the energy spectrum of individual particles near the Fermi level gradually flattens, resulting in a plateau. This flattening of the spectrum is linked to the growth of the effective mass of fermions at the Fermi level (m_F) and a corresponding spike in the density of states (DOS). In this paper, the top valence band flattens upon the application of tensile strain. Flat bands in the valence band maximum (VBM) of a semiconductor can be useful in certain electronic and optoelectronic devices such as LEDs and lasers because they can lead to an increased DOS in the VBM. Along with that, a large spin splitting found in the VBM is understood to extend its promising application in spintronic devices. The dangling bonds of 2D n-vdW materials when cleaved from their bulk counterpart are instrumental for their integration on the surface of other n-vdW 2D or 3D materials. This integration paves the way for numerous industrial applications. In this context, we have demonstrated the compatibility of a ScP monolayer with a silicon substrate and observed that the flat-band feature investigated in this paper remains intact and holds significant advantages when implemented on an electronic industry material such as silicon. It is anticipated that this theoretical study will potentially trigger the experimental synthesis of these structures, leading to the progression of cutting-edge electronic materials and their diverse range of applications.

II. COMPUTATIONAL DETAILS

Density functional theory encoded in VASP [64,65] has been utilized to conduct first-principles calculations. Projected augmented-wave [66] potentials have been employed to describe the interaction among ions and electrons, while the GGA-PBE [67] functionals have been utilized to calculate exchange-correlation functionals. To avoid the underestimation of band gaps by PBE and to ensure the reliable computation of electronic properties, the screened hybrid HSE06 [68] has been implemented by replacing 25% of the exchange-interaction from GGA-PBE with that of HSE06 functionals. The expansion of wave functions has been carried out with an energy cutoff of 500 eV, and both atoms and unit cell have been fully relaxed until the Hellmann-Feynman forces on them reach $< 0.01\,\mathrm{eV/Å}$. The convergence criteria for self-consistent calculations have been set to 10^{-8}eV. The Γ-centered k-mesh of sizes $12 \times 12 \times 1$ has been utilized to sample the hexagonal Brillouin zone. To minimize interactions between periodic images, a vacuum thickness of ~22 Å has been maintained along the z direction. Phonon dispersion curves have been obtained using density functional perturbation theory incorporated into the PHONOPY code [69] for a $5 \times 5 \times 1$ k-mesh employing a $2 \times 2 \times 1$ supercell with 8 atoms. To validate the thermal stability of ScX monolayers, *ab initio* molecular dynamics (AIMD) simulations are conducted at room temperature $T_0 = 300\,\mathrm{K}$ using a time step of 5 ps. A Nosé-Hoover thermostat [70], implemented in VASP, is employed for temperature control. Finally, the finite differences method available with VASP has been employed

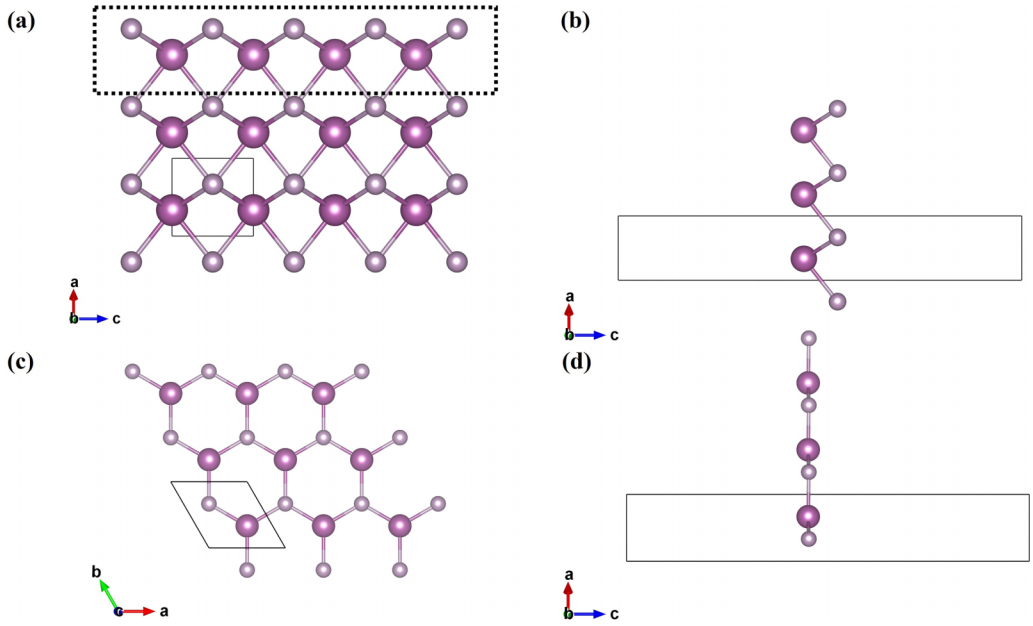

FIG. 1. (a) Bulk three-dimensional (3D) counterpart of ScX (X = P, As, Sb). (b) Side view of exfoliated buckled ScX in two dimensions (2D). (c) and (d) Top and side views of 1-atom-thick planar ScX.

to calculate the elastic stiffness moduli for the relaxed ions. The DFPT method integrated in VASP was used to determine the relaxed-ion piezoelectric stress coefficients by combining the ionic and electronic contributions [71].

III. RESULTS AND DISCUSSIONS

The exfoliation of n-vdW 2D materials is orientation dependent due to their vectorial physical properties. Two layers, one each of Sc and X (X = P, As, Sb) atoms, have been taken from the bulk wurtzite cell of ScX [Fig. 1(a)] in the direction [0 0 1] and put in a unit cell with a vacuum thickness of 20 Å, which is the buckled 2D hexagonal ScX (h-ScX), as can be seen in Fig. 1(b). Relaxing only ions, the wurtzite-derived buckled phase ScP is found to be higher in energy than the bulk counterpart by 1.17 eV and dynamically unstable with a maximum negative/imaginary frequency of $-66\,\mathrm{cm}^{-1}$. After full relaxation of the atoms along with the cell, the buckled monolayers easily get transformed into 1-atom-thick planar graphitic monolayers of h-ScX, the top and side view of which can be seen in Figs. 1(c) and 1(d). The reorganization of atoms in the exfoliated 2D layer can be attributed to the dangling bonds present at the surface. The energy of the optimized graphitic ScP monolayer is lower than the wurtzite-derived 2D layer by 336 meV/atom yet much higher than that of the bulk counterpart. Generally, the exfoliation energies for the n-vdW materials are expected to be higher than that of vdW materials, as the detachment of the layers involves bond breaking [35,72]. The exfoliation energy of the ScX monolayers is calculated in accordance with Ref. [73]. The respective values 0.18, 0.17, and $0.15\,\mathrm{eV/Å}^2$ for ScP, ScAs, and ScSb are found to be comparable with experimentally realized 2D n-vdW binary semiconductor Fe_2O_3 ($\sim$0.14 eV) and other previously reported 2D n-vdW materials [74] and 2-atom-thick ScX monolayers as reported in our previous work [21].

Further, dynamic stability of the planar h-ScX has been checked using phonon dispersion. Softening of the flexural acoustic (ZA) mode along the entire Brillouin zone with the most negative frequencies of -31.68, -18.02, and $-11.67\,\mathrm{cm}^{-1}$ at high-symmetry point M for ScP, ScAs, and ScSb, respectively, as can be seen in Fig. S1 in the Supplemental Material (SM) [75], suggests the dynamic instability of the structures. In general, the structure is optimized in a way to attain the lowest energy and thermodynamically most favorable state of the structure, but in this case, the ground state or the thermodynamically most favorable structure is not dynamically stable. Therefore, a higher-energy state can be pondered. Further, when the monolayers are truncated from the bulk phase, the bond length decreases because of the lost coordination from the bulk phase. The decreased anion-cation distance leads to a Coulomb repulsion between the electron clouds present on the anions and cations. Therefore, extending the ion distances and thus reducing the Coulomb repulsion can be a desirable approach toward the stability of planar graphitic 2D n-vdW monolayers. For that, applying strain would be the first idea adapted. A biaxial tensile strain has thus been applied to the ScX systems. The cohesive energy tends to diminish with the tensile strain, as shown in Fig. S2 in the SM [75], which is okay since we are moving away from the thermodynamically most favorable state. The decreased cohesive energy is still comparable with many presynthesized well-known stable 2D materials [76–79], clearly indicating the maintenance of thermodynamic stability of the 2D monolayers under tensile strain. Nonetheless, there are other vital parameters to be considered for the stability of any system. The thermal stability of the structures at room temperature has been confirmed using AIMD calculations. The calculations were performed with a time step of 1 ps and a temperature of 300 K for a duration of 5 ps, as shown in Fig. S3 in the SM [75]. The structures remained intact throughout the entire simulation period.

Phonon dispersion corroborates stability under a minor strain of +1, +2, and +1% for ScP, ScAs, and ScSb, respectively, which is evidenced by the disappearance of the imaginary phonon modes. The bond distances are increased with higher strain, reducing the Coulomb repulsion among the electrons present in the orbitals of nearby atoms, thereby stabilizing the structures. Nonetheless, the structures are still planar, unlike the previously reported similar structure nonpolar buckled CdS [36]. Taking a closer look at the phonon dispersion of the pristine structures, it is visible that the phonon instability is caused by the out-of-plane flexural acoustic (ZA) mode contributed by the X atom. The non-Γ nature of the deepest phonon instabilities implies that atoms are moving in different directions in adjacent unit cells. The phonon dispersion affirms that the structures are further stable up to a biaxial strain of +13, +14, and +14% for ScP, ScAs, and ScSb, respectively, as can be seen in Figs. S4–S6 in the SM [75]. Another way to stabilize the monolayers is by applying uniaxial tensile strain along the lattice vectors, ensuring the stability up to 20%, as can be seen in Fig. S7 in the SM [75].

The Born-Huang stability criteria, which state that $C_{11}C_{22} - C_{12}^2 > 0$ and $C_{66} > 0$, are satisfied by the elastic constants of strained ScX monolayers, affirming the mechanical stability of these materials. Elevating biaxial strain alleviates the in-plane elastic constants significantly, as can be seen in Table S1 in the SM [75]. The markedly low-elastic coefficient can be ascribed to the ionic nature of the interatomic bonding. These results are indifferent to the choice of the unit cell. We have also conducted these studies on an orthorhombic cell for ScP, and found to be equal to that in the hexagonal unit cell, as evident from the results compared in Tables S1−S3 in the SM [75]. The static Young's moduli of the monolayers ScP (Y_{2D} = 9–20 N/m), ScAs (Y_{2D} = 9–18 N/m), and ScSb (Y_{2D} = 6–14 N/m) are notably diminutive (see Table S2 in the SM [75]) compared with graphene (Y_{2D} = 340 N/m) [80], h-BN (Y_{2D} = 279.2 N/m) [81], MoS_2 (Y_{2D} = 118–141 N/m) [82], phosphorene (Y_{2D} = 23.0–92.3 N/m) [83,84], and silicene (Y_{2D} = 60 N/m) [85,86], implying a high degree of flexibility and thereby inspiring for the investigation of applications of in-plane strain engineering. Additionally, to assess the stretchability of t-ScX nanosheets, we investigated the stress-strain relationship for strain applied along both the x and y directions, with a maximum strain of 25%. As strain is introduced, stress gradually builds up on the surface of the nanosheets until it reaches the ultimate stress point or failure stress, at which point the material begins to rupture. The stretchability of the material is directly linked to the magnitude of the ultimate stress point. To determine the true stress in GPa (N/m^2), VASP utilizes 3D periodic boundary conditions. Consequently, it is necessary to scale or renormalize the 2D elastic stiffness constants by the z lattice constant or supercell thickness. This can be achieved through the equation $C_{3D} = C_{2D}/c$, where $C_{3D\,(2D)}$ represents the 3D (2D) elastic stiffness constant, and c denotes the z lattice constant or supercell thickness [41]. The ultimate strain limits for the monolayers are as high as 16–24%, as can be seen in Fig. S8 in the SM [75]. The flexibility and ability to withstand deformation without failure contribute to the durability and reliability of materials. High ultimate strain allows materials to undergo significant elongation or compression before reaching their breaking point, making them suitable for applications where deformation resistance is crucial. Additionally, materials with high ultimate strain can exhibit improved formability and shape adaptability, making them easier to process and mold into complex shapes. The ultimate strengths of the monolayers are comparable with that of phosphorene (10 N/m) [87].

Therefore, the mode-dependent stable phonon dispersions are analyzed further for ScP, as can be seen in Fig. S9 in the SM [75]. The in-plane longitudinal optical (LO) and transverse optical (TO) modes lower in energy, while the out-of-plane optical (ZO) mode rises in energy with tensile strain. Therefore, a decreasing energy gap between the TO and ZO modes is observed, which further vanishes followed by the overlapping of the optical modes. There is a visible mixing of in-plane optical and acoustic phonon modes at strain >9% caused by the complex crossing of the phonon branches, which is generally found in systems having several constituent atoms in their unit cell. Due to the mixing of phonon modes, the excitation of one phonon will impact the other. The process of interaction of electrons with phonons can be related to both optical and acoustic modes simultaneously. Therefore, the interaction of electrons with the lattice would be interesting to study. The optical phonon modes acquire lower frequencies with the tensile strain, leading to a cogent mixing of phonon branches. The TO mode is found to mix with longitudinal acoustic (LA) and transverse acoustic (TA) modes, as can be seen in Fig. 2 when a certain aspect of lattice strain interacts with relative sublattice oscillation. This interaction occurs because not all the constituent atoms occupy the center of symmetry with potential consequences for piezoelectric and sublattice-piezoelectric effects. Concurrently, strong electron-phonon coupling is expected due to the complex mixing of LA, TA, and TO modes, suggesting a large value of the piezoelectric constant and, therefore, a large piezoelectric strain coefficient (PSC). Piezoelectricity is analyzed with tensile strain and the shear PSC d_{16} shows significant enhancement in magnitude. In-plane piezoelectric constants d_{21} and d_{22} accompany d_{16}, though d_{22} increases in the positive direction, while d_{16} and d_{21} increase in the negative direction, as shown in Fig. 3. The arousal of negative signs of d_{16} and d_{21} after +3% strain is attributed to the dominance of electronic contribution over the ionic. The equal-in-magnitude-but-opposite-in-sign in d_{21} and d_{22} represents the opposite shifts of the ions under tensile strain.

For a 2D hexagonal structure, the d_{16} piezoelectric constant represents the change in the electrical polarization of a material along the x axis, per unit area, per unit shear stress applied in the xy plane, a schematic of which is shown in Fig. 4. In other words, d_{16} is used to study the behavior of the material when it is subjected to longitudinal-transverse stress in the xy plane. The high increase in the magnitude of d_{16} is thus well aligned with the complex mixing of LA, TA, and TO modes. The values of d_{16} have been increased to as high as $d_{16} = -228.08$, −469.87, and −397.52 pm/V in ScP, ScAs, and ScSb, respectively, through tensile strain, which is much higher than in bulk 3R-TMDCs ($MoS_2 = -8.3$ pm/V, $MoSe_2 = -10.3$ pm/V, $WS_2 = -5.1$ pm/V, and $WSe_2 = -7.0$ pm/V) [88], $BiB_3O_6 = 13.9$ pm/V [89], and even amino acids (asparagine = 13 pm/V, histidine = 18 pm/V, leucine = 12.5 pm/V, and glycine = 178 pm/V) [49,90].

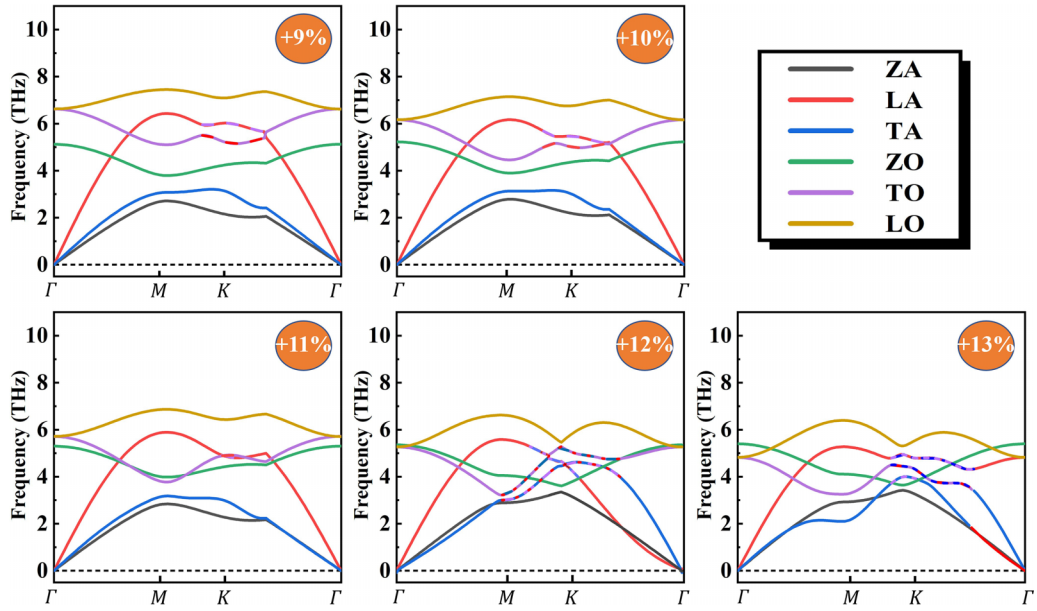

FIG. 2. Phonon dispersion of ScP with tensile strain +9 to +13%. Visible complex mixing of longitudinal acoustic (LA), transverse acoustic (TA), and transverse optical (TO) phonon modes.

With that, the d_{15} piezoelectric constant which represents the change in the electrical polarization of a material along the x axis, per unit area, per unit shear stress applied about the y direction or in the xz plane, is sufficiently high and can be easily tuned via tensile strain in the range −90 to 210 pm/V, as can be seen in Fig. S10 in the SM [75]. The high values of shear piezoelectric coefficients of 2D planar hexagonal structures can be used to create highly sensitive sensors for detecting changes in mechanical stress, pressure, and force and also in actuators, energy harvesting, filtering and medical devices, and pressure sensors [49–54,91,92]. However, more research is needed to understand the properties and behaviors of the structures to develop practical applications. Again, the trend in the tuning of the piezoelectric constants through positive strain remains unaffected by the choice of the unit cell. The results obtained from the orthorhombic cell (Fig. S11 in the SM [75]) can be compared with those obtained from the hexagonal cell for ScP (Fig. 3).

The ZO mode arises by the swing of Sc and X atoms in vertically opposite directions. That is, if the Sc atom is moving in the up direction, the neighboring X atoms will be moving in the down direction, which generates a time-varying electrical dipole moment in the direction perpendicular to the plane of the monolayer. With the expansion of the unit cell along the in-plane directions, the frequency of oscillation increases in the out-of-plane direction. The out-of-plane oscillations (ZO) achieve a higher frequency than the in-plane oscillations (LO and TO) $>\sim$13% and thus cause the time-varying dipole moment in the perpendicular direction of the plane of the monolayer to increase, thereby leading to instability in the system again which is seen by the presence of soft TA modes. The stability of these graphitic ScX monolayers with a vast range of tensile strains points to their suitability for different heterostructure formations and for use on different substrates.

Further, the effect of biaxial tensile strain on the electronic structure of the 1-atom-thick scandium pnictides has been examined. The unstrained unstable structure of the ScX structures possess a direct band gap at the K point (see Fig. S12 in the SM [75]), which remains direct on the application of biaxial strain. There is an interesting shift in the

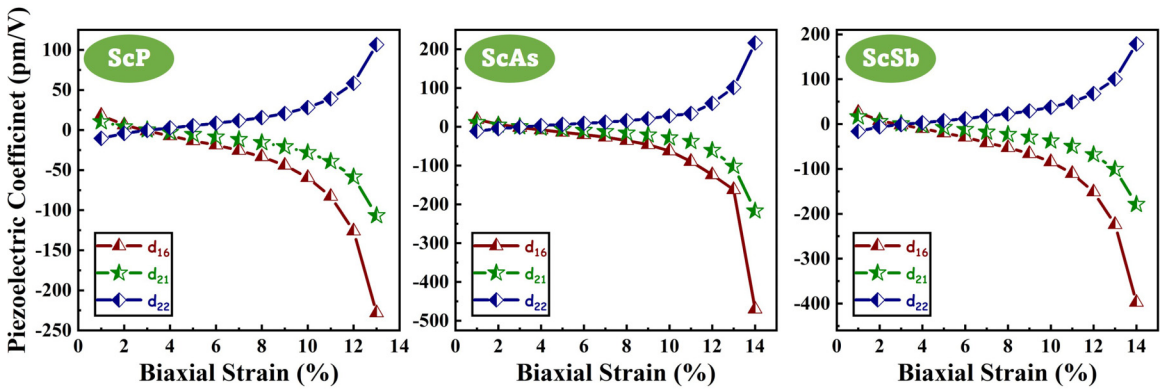

FIG. 3. Variation of piezoelectric coefficients, d_{16}, d_{21}, and d_{22} of ScX (X = P, As, Sb) with biaxial strain up to 13%.

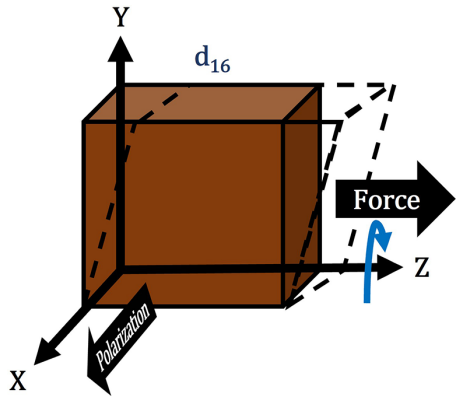

FIG. 4. Stress about the z direction or in the xy plane, causing polarization in the x direction.

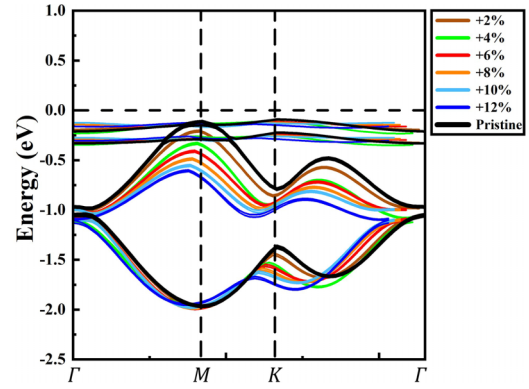

FIG. 6. Splitting of nearly flat top-most valence band in ScP monolayer.

energy of the bands in the valence band. This shift can be understood by scrutinizing the contribution of different orbitals in the band edges. It is observed that the parabolic inverted-valleylike band is contributed by in-plane orbitals (Sc_px, Sc_py, Sc_dxy, Sc_dx2, P_px, and P_py), while the nearly flat bands are contributed by the out-of-plane orbitals (Sc_dyz, Sc_dxz, and P_pz). The former band is evidently sensitive to the application of in-plane tensile strain, owing to its orbital composition. As a result, with the application of in-plane tensile strain, the parabolic inverted-valleylike band is lowered in energy, leaving the nearly flat band as the top-most valence band, as can be seen in Fig. 5(a). Further, it is succinct from Fig. 5(b) that the nearly flat bands become more flattened with tensile strain. The fundamental physics here can be well understood from the renowned Kronig-Penny model [93]. According to the model, the bandwidth of a certain band is given by the relationship $W = 1/(V_0 ba)^2$, where a and b are the widths of the potential well and the barrier, or correspondingly, the lattice period, respectively. Biaxial tensile strain stretches the in-plane lattice vectors and, therefore, suppresses the bandwidth. In solids, the kinetic energy and the electron correlation effects are associated with the bandwidth. Thus, the lowering of the bandwidth gives rise to flat bands near the Fermi level isolated from other valence bands. These flat bands are also tunable within the wide range of biaxial tensile strain. Systems with flat bands around the Fermi level provide intriguing environments for investigating the fascinating physics of strong electron correlations [94]. Furthermore, flat valence bands indicate a higher effective mass of holes that can be useful in semiconductor devices such as solar cells, where the heavier holes can be more easily collected and used to generate electrical power. Additionally, materials with higher effective mass of holes can be used in thermoelectric devices to convert waste heat into electricity. In electronic devices, high effective mass of holes also leads to greater electron-hole recombination rate, which is useful in LED and lasing devices.

A large splitting in flat bands of the order of 100 meV is observed while including relativistic corrections (Fig. 6). The splitting of flat bands in the VBM of a semiconductor can be beneficial for certain electronic devices due to the increase in DOS in the VBM. Furthermore, the increased DOS can lead to increased optical absorption and improved performance in optoelectronic devices, such as LEDs and lasers. Additionally, the splitting of flat bands can lead to increased spin-polarization and improved spin-dependent transport properties, which can be useful for spintronic devices, such as magnetic random-access memories (MRAMs) and spin-field-effect transistors (spin-FETs) that rely on the spin of electrons and holes to perform their functions. As anticipated in earlier studies, the band dispersion differs between

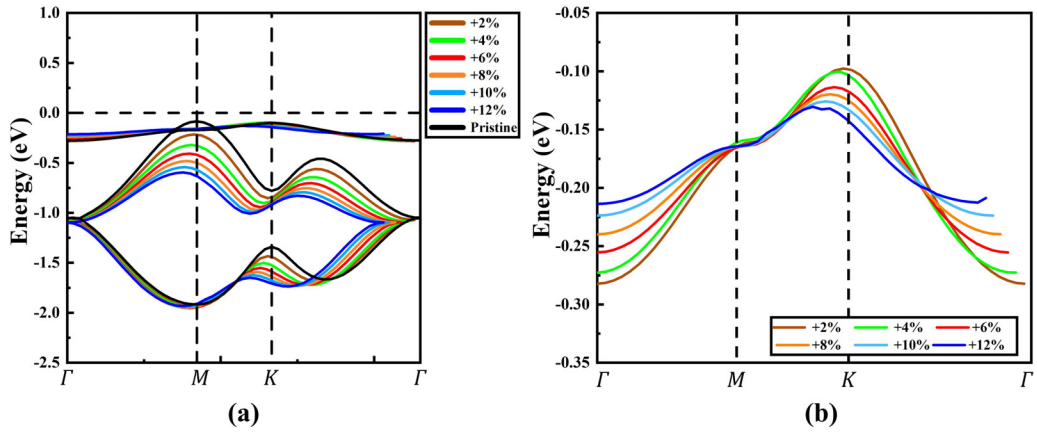

FIG. 5. (a) Valence band variation in ScP with tensile strain up to +12%. (b) Top valence band flattening with strain.

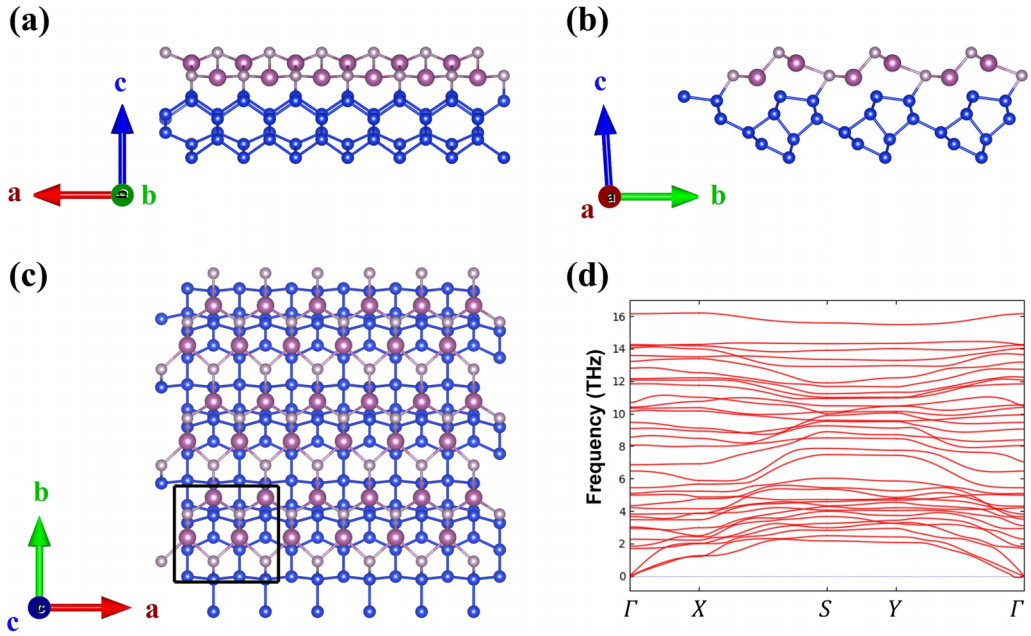

FIG. 7. ScP monolayer on Si substrate: (a) and (b) side view, (c) top view, and (d) phonon dispersion.

the orthorhombic and hexagonal cells [95–98]. However, the change in electronic structure upon the application of biaxial tensile strain is invariant with respect to the choice of unit cell, as demonstrated in Figs. 5 and S13 in the SM [75].

Significantly, an intriguing advantage arises from the simultaneous presence of flat bands and piezoelectricity. Piezoelectricity is a phenomenon where the material can generate an electric charge in response to applied mechanical stress or strain. The more the electrical charge, the stronger the piezoelectric response will be. The flat band resulting from high DOS in the VBM can contribute to this enhanced piezoelectric response by making more charge carriers available in a small energy range under strain, leading to a more efficient conversion of mechanical energy into electrical energy. Both the flattening of the bands and piezoelectricity are found to increase with strain. Therefore, the presence of a flat band in a material can be linked to the observed large piezoelectricity, suggesting that the unique electronic structure associated with the flat band plays a crucial role in enhancing the piezoelectric properties of the material.

Further, the ability of these monolayers to withstand high strain along different directions makes them suitable for supporting them on different substrates and in various heterostructures. The unstrained ScP monolayer is dynamically stable when implanted on the Si substrate (Fig. 7) and therefore will manifest strong integration capability with Si-based electronic devices. The stability of these monolayers on a Si substrate lays the foundation for their successful implementation in various technological domains, unlocking possibilities and opportunities for innovation of a wide range of practical nanodevice applications, including but not limited to electronics, optics, and energy storage [99–101].

Further, it is evident from Fig. 7 that ScP implanted on silicon exhibits chemical bonding instead of vdW attraction. Consequently, the resulting structure of ScP/Si may possess distinct properties as compared with ScP or Si individually. On that ground, we have examined the impact of Si substrate on the ScP monolayer. It is interesting to note that the introduction of the ScP monolayer onto the Si substrate results in a notable flat band structure and a substantial enhancement in the DOS near the Fermi level, as can be seen in Fig. 8.

While we note the preservation of the investigated flat band feature, which offers significant advantages when implemented on an electronic industry material like silicon, it is worth mentioning that the implantation of ScP on a silicon substrate induces a strain of 4.6% due to the lattice mismatch. Consequently, we conducted a comprehensive comparison of the piezoelectric properties between two strained systems: one involving the combined ScP-Si system where ScP is strained by 4.6% due to the silicon substrate and the other with freestanding strained ScP with 4.6% strain, which was achieved computationally through biaxial strain. Notably, the shear piezoelectric coefficient d_{16}, which holds particular interest in the ScP monolayer, exhibits a remarkable threefold enhancement when implanted on silicon. This conclusion was drawn by comparing the d_{16} values of ScP-Si (-37.19 pm/V) and ScP at 4.6% strain (-10.52 pm/V). The piezoelectric coefficients d_{16}, d_{21}, and d_{22} for freestanding strained ScP at 4.6% strain were obtained by interpolating the piezoelectric variation curve under strain. The in-plane piezoelectric coefficients d_{21} (-1.33 pm/V) and d_{22} (0.40 pm/V) in ScP-Si are reduced compared with ScP ($d_{21} = -3.11$ pm/V, $d_{22} = 3.11$ pm/V). The detailed explanation and comparison for this is provided in the SM [75]. Evidently, there are more flat bands in ScP-Si relative to freestanding ScP. Concurrently, there is a threefold enhancement in the shear piezoelectric coefficient d_{16}. This demonstrates a clear relationship between flat bands and high shear piezoelectricity.

IV. CONCLUSIONS

In this paper, 1-atomic-layer-thick graphitic n-vdW monolayers of ScX (X = P, As, Sb) has been stabilized via the

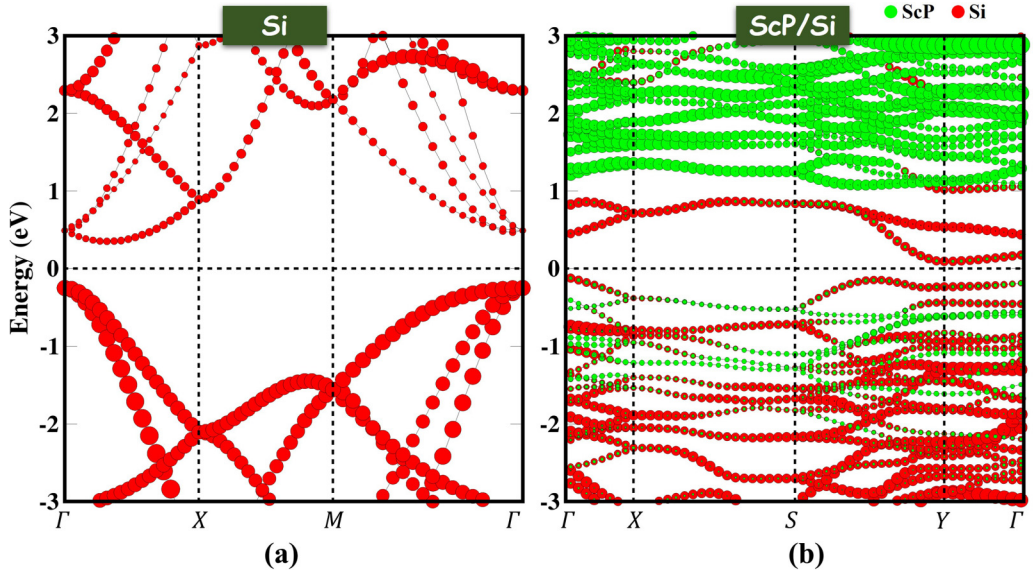

FIG. 8. Band structure of (a) bulk Si and (b) ScP/silicon using PBE functional indicating band flattening by the imposition of ScP monolayer on silicon.

application of minute tensile strain whose stability has been confirmed over a vast range of biaxial strain (∼13–14%) and uniaxial strain (∼20%). The monolayers possess high flexibility due to their exceptionally low in-plane elastic constants (6–43 N/m) and Young's modulus (6–20 N/m) arising from the predominance of ionic interatomic bonding. Therefore, they are proposed for applications where large-scale strain engineering is needed. To investigate their potential, the mode-dependent phonon dispersion, electronic structure, and piezoelectric properties of the ScX monolayer were studied under tensile strain. High shear piezoelectric coefficients are attained up to $d_{16} = -228.08$, -469.87, and -397.52 pm/V for ScP, ScAs, and ScSb, respectively, opening a path for pressure sensors and several biomedical applications. Moreover, excellent tuning via strain can be achieved in the shear piezoelectric coefficient d_{15} that can be useful in actuators and resonators. The application of tensile strain flattens the top valence band, accompanied by a spin splitting of ∼100 meV, resulting in strong fermion-fermion correlation effects. This indicates a higher effective mass of holes, which is exploitable in semiconductor devices such as solar cells, where heavier holes can be more easily collected and used to generate electrical power. Furthermore, this feature leads to a greater electron-hole recombination rate, which is beneficial for LEDs and lasing devices. These monolayers have promising applications in MRAMs and spin-FETs, which rely on the spin of electrons and holes to perform their functions. In addition, their ability to withstand high strain makes them suitable for integrability with various substrates and in different heterostructures. The ScP monolayer exhibited robust stability and maintained its flat band characteristic when implanted on a Si substrate, thereby opening opportunities for innovation in a wide range of practical applications. These findings demonstrate the potential of the ScP monolayer for futuristic applications in the field of strain engineering and semiconductor device design.

ACKNOWLEDGMENTS

The Council of Scientific and Industrial Research with Grant No. 09/1129(0030)/2020-EMR-I and University Grant Commission, India with Grant No. 211610021376, are acknowledged by the authors for their financial support. The authors express gratitude to the Institute of Nano Science and Technology, Mohali, India, for offering supercomputing facilities on their in-house high-performance computing cluster as well as infrastructure and fellowship support. The authors also gratefully acknowledge the supercomputing resources and support provided by Center for Development of Advanced Computing, Pune, on PARAM Smriti and PARAM Shivay under the National Supercomputing Mission, Government of India, at National Agri-Food Biotechnology Institute, Mohali, and the Indian Institute of Technology, Varanasi, respectively.

[1] K. S. Novoselov, A. K. Geim, S. V. Morozov, D. Jiang, Y. Zhang, S. V. Dubonos, I. V. Grigorieva, and A. A. Firsov, Electric field effect in atomically thin carbon films, Science **306**, 666 (2004).

[2] J. Dai and X. C. Zeng, Titanium trisulfide monolayer: Theoretical prediction of a new direct-gap semiconductor with high and anisotropic carrier mobility, Angew. Chemie Int. Ed. **127**, 7682 (2015).

[3] P. Li, W. Zhang, C. Liang, and X. C. Zeng, Two-dimensional MgX_2Se_4 (X = Al, Ga) monolayers with tunable electronic properties for optoelectronic and photocatalytic applications, Nanoscale **11**, 19806 (2019).

[4] M. Qiao, J. Liu, Y. Wang, Y. Li, and Z. Chen, $PdSeO_3$ monolayer: Promising inorganic 2D photocatalyst for direct overall water splitting without using sacrificial reagents and cocatalysts, J. Am. Chem. Soc. **140**, 12256 (2018).

[5] P. Zhao, Y. Ma, X. Lv, M. Li, B. Huang, and Y. Dai, Two-dimensional III2-VI3 materials: Promising photocatalysts for overall water splitting under infrared light spectrum, Nano Energy **51**, 533 (2018).

[6] Z. Guo, J. Zhou, L. Zhu, and Z. Sun, MXene: A promising photocatalyst for water splitting, J. Mater. Chem. A **4**, 11446 (2016).

[7] P. Ganguly, M. Harb, Z. Cao, L. Cavallo, A. Breen, S. Dervin, D. D. Dionysiou, and S. C. Pillai, 2D nanomaterials for photocatalytic hydrogen production, ACS Energy Lett. **4**, 1687 (2019).

[8] H. Liu, A. T. Neal, Z. Zhu, Z. Luo, X. Xu, D. Tománek, and P. D. Ye, Phosphorene: An unexplored 2D semiconductor with a high hole mobility, ACS Nano **8**, 4033 (2014).

[9] M. Xie, S. Zhang, B. Cai, Z. Zhu, Y. Zou, and H. Zeng, Two-dimensional BX (X = P, As, Sb) semiconductors with mobilities approaching graphene, Nanoscale **8**, 13407 (2016).

[10] M. K. Mohanta, H. Seksaria, and A. De Sarkar, Insights into CrS_2 monolayer and n-CrS_2/p-HfN_2 interface for low-power digital and analog nanoelectronics, Appl. Surf. Sci. **579**, 152211 (2022).

[11] G.-B. Liu, D. Xiao, Y. Yao, X. Xu, and W. Yao, Electronic structures and theoretical modelling of two-dimensional group-VIB transition metal dichalcogenides, Chem. Soc. Rev. **44**, 2643 (2015).

[12] A. Gupta, T. Sakthivel, and S. Seal, Recent development in 2D materials beyond graphene, Prog. Mater. Sci. **73**, 44 (2015).

[13] B. Luo, G. Liu, and L. Wang, Recent advances in 2D materials for photocatalysis, Nanoscale **8**, 6904 (2016).

[14] Y. Li, Y. L. Li, B. Sa, and R. Ahuja, Review of two-dimensional materials for photocatalytic water splitting from a theoretical perspective, Catal. Sci. Technol. **7**, 545 (2017).

[15] A. Kishore, N. Tripathy, and A. De Sarkar, Unconventional anisotropy in excitonic properties and carrier mobility in iodine-based XTeI (X = Ga, In) monolayers for visible-light photocatalytic water splitting, J. Phys. Chem. C **127**, 1992 (2022).

[16] X. Yu, T. J. Marks, and A. Facchetti, Metal oxides for optoelectronic applications, Nat. Mater. **15**, 383 (2016).

[17] P. Kumbhakar, C. Chowde Gowda, P. L. Mahapatra, M. Mukherjee, K. D. Malviya, M. Chaker, A. Chandra, B. Lahiri, P. M. Ajayan, D. Jariwala *et al.*, Emerging 2D metal oxides and their applications, Mater. Today **45**, 142 (2021).

[18] A. Puthirath Balan, S. Radhakrishnan, C. F. Woellner, S. K. Sinha, L. Deng, C. D. L. Reyes, B. M. Rao, M. Paulose, R. Neupane, A. Apte *et al.*, Exfoliation of a non–van der Waals material from iron ore hematite, Nat. Nanotechnol. **13**, 602 (2018).

[19] A. Puthirath Balan, S. Radhakrishnan, R. Kumar, R. Neupane, S. K. Sinha, L. Deng, C. A. De Los Reyes, A. Apte, B. M. Rao, M. Paulose *et al.*, A non–van der Waals two-dimensional material from natural titanium mineral ore ilmenite, Chem. Mater. **30**, 5923 (2018).

[20] T. P. Yadav, S. N. Shirodkar, N. Lertcumfu, S. Radhakrishnan, F. N. Sayed, K. D. Malviya, G. Costin, R. Vajtai, B. I. Yakobson, C. S. Tiwary *et al.*, Chromiteen: A new 2D oxide magnetic material from natural ore, Adv. Mater. Interfaces **5**, 1800549 (2018).

[21] H. Seksaria, A. Kaur, K. Singh, and A. De Sarkar, Hexagonal and tetragonal ScX (X = P, As, Sb) nanosheets for optoelectronics and straintronics, Appl. Surf. Sci. **615**, 156306 (2023).

[22] A. B. Puthirath, S. N. Shirodkar, G. Gao, F. C. R. Hernandez, L. Deng, R. Dahal, A. Apte, G. Costin, N. Chakingal, A. P. Balan *et al.*, Scale-enhanced magnetism in exfoliated atomically thin magnetite sheets, Small **16**, 2004208 (2020).

[23] A. B. Puthirath, A. P. Balan, E. F. Oliveira, V. Sreepal, F. C. Robles Hernandez, G. Gao, N. Chakingal, L. M. Sassi, P. Thibeorchews, G. Costin *et al.*, Apparent gerromagnetism in exfoliated ultrathin pyrite sheets, J. Phys. Chem. C **125**, 18927 (2021).

[24] M. G. Moinuddin, S. Srinivasan, and S. K. Sharma, Probing ferrimagnetic semiconductor with enhanced negative magnetoresistance: 2D chromium sulfide, Adv. Electron. Mater. **7**, 2001116 (2021).

[25] L. Hu, L. Cao, L. Li, J. Duan, X. Liao, F. Long, J. Zhou, Y. Xiao, Y. J. Zeng, and S. Zhou, Two-dimensional magneto-photoconductivity in non–van der Waals manganese selenide, Mater. Horizons **8**, 1286 (2021).

[26] A. Yousaf, M. S. Gilliam, S. L. Y. Chang, M. Augustin, Y. Guo, F. Tahir, M. Wang, A. Schwindt, X. S. Chu, D. O. Li *et al.*, Exfoliation of quasi-two-dimensional nanosheets of metal diborides, J. Phys. Chem. C **125**, 6787 (2021).

[27] Y. Guo, A. Gupta, M. S. Gilliam, A. Debnath, A. Yousaf, S. Saha, M. D. Levin, A. A. Green, A. K. Singh, and Q. H. Wang, Exfoliation of boron carbide into ultrathin nanosheets, Nanoscale **13**, 1652 (2021).

[28] C. Gibaja, D. Rodríguez-San-Miguel, W. S. Paz, I. Torres, E. Salagre, P. Segovia, E. G. Michel, M. Assebban, P. Ares, D. Hernández-Maldonado *et al.*, Exfoliation of alpha-germanium: A covalent diamond-like structure, Adv. Mater. **33**, 2006826 (2021).

[29] Y. Wei, M. Ghorbani-Asl, and A. V. Krasheninnikov, Tailoring the electronic and magnetic properties of hematene by surface passivation: Insights from first-principles calculations, J. Phys. Chem. C **124**, 22784 (2020).

[30] C. Jin and L. Kou, Two-dimensional non–van der Waals magnetic layers: Functional materials for potential device applications, J. Phys. D: Appl. Phys. **54**, 413001 (2021).

[31] A. C. M. Padilha, M. Soares, E. R. Leite, and A. Fazzio, Theoretical and experimental investigation of 2D hematite, J. Phys. Chem. C **123**, 16359 (2019).

[32] R. I. Gonzalez, J. Mella, P. Diaz, S. Allende, E. E. Vogel, C. Cardenas, and F. Munoz, Hematene: A 2D magnetic material in van der Waals or non–van der Waals heterostructures, 2D Mater. **6**, 045002 (2019).

[33] A. Bandyopadhyay, N. C. Frey, D. Jariwala, and V. B. Shenoy, Engineering magnetic phases in two-dimensional non–van der Waals transition-metal oxides, Nano Lett. **19**, 7793 (2019).

[34] M. Nakhaee, M. Yagmurcukardes, S. A. Ketabi, and F. M. Peeters, Single-layer structures of A100- and B010-gallenene: A tight-binding approach, Phys. Chem. Chem. Phys. **21**, 15798 (2019).

[35] A. P. Balan, A. B. Puthirath, S. Roy, G. Costin, E. F. Oliveira, M. A. S. R. Saadi, V. Sreepal, R. Friedrich, P. Serles, A. Biswas *et al.*, Non–van der Waals quasi-2D materials;

Recent advances in synthesis, emergent properties and applications, Mater. Today **58**, 164 (2022).
[36] P. Kumari, S. Debnath, and P. Mahadevan, Structural distortions in monolayers of binary semiconductors, Phys. Rev. B **97**, 041404(R) (2018).
[37] K. Kaur, D. Murali, and B. R. K. Nanda, Stretchable and dynamically stable promising two-dimensional thermoelectric materials: ScP and ScAs, J. Mater. Chem. A **7**, 12604 (2019).
[38] E. Nasr Esfahani, T. Li, B. Huang, X. Xu, and J. Li, Piezoelectricity of atomically thin WSe_2 via laterally excited scanning probe microscopy, Nano Energy **52**, 117 (2018).
[39] L. C. Gomes, A. Carvalho, and A. H. Castro Neto, Enhanced piezoelectricity and modified dielectric screening of two-dimensional group-IV monochalcogenides, Phys. Rev. B **92**, 214103 (2015).
[40] K. A. N. Duerloo, M. T. Ong, and E. J. Reed, Intrinsic piezoelectricity in two-dimensional materials, J. Phys. Chem. Lett. **3**, 2871 (2012).
[41] M. N. Blonsky, H. L. Zhuang, A. K. Singh, and R. G. Hennig, *Ab initio* prediction of piezoelectricity in two-dimensional materials, ACS Nano **9**, 9885 (2015).
[42] N. Jena Dimple, A. Rawat, R. Ahammed, M. K. Mohanta, and A. De Sarkar, Emergence of high piezoelectricity along with robust electron mobility in Janus structures in semiconducting group IVB dichalcogenide monolayers, J. Mater. Chem. A **6**, 24885 (2018).
[43] Q. Zhang, S. Zuo, P. Chen, and C. Pan, Piezotronics in two-dimensional materials, InfoMat. **3**, 987 (2021).
[44] H. Zhu, Y. Wang, J. Xiao, M. Liu, S. Xiong, Z. J. Wong, Z. Ye, Y. Ye, X. Yin, and X. Zhang, Observation of piezoelectricity in free-standing monolayer MoS_2, Nat. Nanotechnol. **10**, 151 (2015).
[45] W. Wu, L. Wang, Y. Li, F. Zhang, L. Lin, S. Niu, D. Chenet, X. Zhang, Y. Hao, T. F. Heinz, J. Hone, and Z. L. Wang, Piezoelectricity of single-atomic-layer MoS_2 for energy conversion and piezotronics, Nature (London) **514**, 470 (2014).
[46] R. Fei, W. Li, J. Li, and L. Yang, Giant piezoelectricity of monolayer group IV monochalcogenides: SnSe, SnS, GeSe, and GeS, Appl. Phys. Lett. **107**, 173104 (2015).
[47] Y. Dai, X. Zhang, Y. Cui, M. Li, Y. Luo, F. Jiang, R. Zhao, and Y. Huang, Theoretical insights into strong intrinsic piezoelectricity of blue-phosphorus-like group-IV monochalcogenides, Nano Res. **15**, 209 (2022).
[48] S. Muensit, E. M. Goldys, and I. L. Guy, Shear piezoelectric coefficients of gallium nitride and aluminum nitride, Appl. Phys. Lett. **75**, 3965 (1999).
[49] S. Guerin, A. Stapleton, D. Chovan, R. Mouras, M. Gleeson, C. McKeown, M. R. Noor, C. Silien, F. M. F. Rhen, A. L. Kholkin *et al.*, Control of piezoelectricity in amino acids by supramolecular packing, Nat. Mater. **17**, 180 (2017).
[50] E. S. Hosseini and R. Dahiya, *Biodegradable Amino Acid-Based Pressure Sensor* (IEEE SENSORS, Rotterdam, Netherlands, 2020), pp. 1–4.
[51] R. Lay, G. S. Deijs, and J. Malmström, The intrinsic piezoelectric properties of materials—A review with a focus on biological materials, RSC Adv. **11**, 30657 (2021).
[52] E. Markgraf, Organic piezoelectric wearable and implantable sensors, URMSE **2**, 42 (2021).
[53] X. Qing, W. Li, Y. Wang, and H. Sun, Piezoelectric transducer-based structural health monitoring for aircraft applications, Sensors **19**, 545 (2019).
[54] X. Gao, X. Xin, J. Wu, Z. Chu, and S. Dong, A multilayered-cylindrical piezoelectric shear actuator operating in shear (d_{15}) mode, Appl. Phys. Lett. **112**, 152902 (2018).
[55] M. Minary-Jolandan and M. F. Yu, Uncovering nanoscale electromechanical heterogeneity in the subfibrillar structure of collagen fibrils responsible for the piezoelectricity of bone, ACS Nano **3**, 1859 (2009).
[56] E. Fukada, Piezoelectricity as a fundamental property of wood, Wood Sci. Technol. **2**, 299 (1968).
[57] E. Fukada and Y. Ando, Piezoelectricity in oriented DNA films, J. Polym. Sci. A **10**, 565 (1972).
[58] M. Smith and S. Kar-Narayan, Piezoelectric polymers: Theory, challenges and opportunities, Int. Mater. Rev. **67**, 65 (2022).
[59] P. Nandi, A. Rawat, R. Ahammed, N. Jena, and A. De Sarkar, Group-IV(A) Janus dichalcogenide monolayers and their interfaces straddle gigantic shear and in-plane piezoelectricity, Nanoscale **13**, 5460 (2021).
[60] V. R. Shaginyan, A. Z. Msezane, J. W. Clark, G. S. Japaridze, and Y. S. Leevik, Universal *T*/*B* scaling behavior of heavy fermion compounds (brief review), JETP Lett. **112**, 657 (2020).
[61] A. Camjayi, K. Haule, V. Dobrosavljević, and G. Kotliar, Coulomb correlations and the Wigner-Mott transition, Nat. Phys. **4**, 932 (2008).
[62] D. Yudin, D. Hirschmeier, H. Hafermann, O. Eriksson, A. I. Lichtenstein, and M. I. Katsnelson, Fermi Condensation Near van Hove Singularities within the Hubbard Model on the Triangular Lattice, Phys. Rev. Lett. **112**, 070403 (2014).
[63] Y. Cao, V. Fatemi, S. Fang, K. Watanabe, T. Taniguchi, E. Kaxiras, and P. Jarillo-Herrero, Unconventional superconductivity in magic-angle graphene superlattices, Nature **556**, 43 (2018).
[64] G. Kresse and J. Furthmüller, Efficiency of *ab-initio* total energy calculations for metals and semiconductors using a plane-wave basis set, Comput. Mater. Sci. **6**, 15 (1996).
[65] G. Kresse and J. Furthmüller, Efficient iterative schemes for *ab initio* total-energy calculations using a plane-wave basis set, Phys. Rev. B **54**, 11169 (1996).
[66] G. Kresse and D. Joubert, From ultrasoft pseudopotentials to the projector augmented-wave method, Phys. Rev. B **59**, 1758 (1999).
[67] J. P. Perdew, K. Burke, and M. Ernzerhof, Generalized Gradient Approximation Made Simple, Phys. Rev. Lett **77**, 3865 (1996).
[68] A. V. Krukau, O. A. Vydrov, A. F. Izmaylov, and G. E. Scuseria, Influence of the exchange screening parameter on the performance of screened hybrid functionals, J. Chem. Phys. **125**, 224106 (2006).
[69] A. Togo and I. Tanaka, First principles phonon calculations in materials science, Scr. Mater. **108**, 1 (2015).
[70] S. Nose, Constant-temperature molecular dynamics, J. Phys. Condens. Matter **2**, SA115 (1990).
[71] X. Wu, D. Vanderbilt, and D. R. Hamann, Systematic treatment of displacements, strains, and electric fields in density-functional perturbation theory, Phys. Rev. B **72**, 035105 (2005).

[72] P. Tao, S. Yao, F. Liu, B. Wang, F. Huang, and M. Wang, Recent advances in exfoliation techniques of layered and non-layered materials for energy conversion and storage, J. Mater. Chem. A **7**, 23512 (2019).

[73] J. H. Jung, C. H. Park, and J. Ihm, A rigorous method of calculating exfoliation energies from first principles, Nano Lett. **18**, 2759 (2018).

[74] R. Friedrich, M. Ghorbani-Asl, S. Curtarolo, and A. V. Krasheninnikov, Data-driven quest for two-dimensional non–van der Waals materials, Nano Lett. **22**, 989 (2022).

[75] See Supplemental Material at http://link.aps.org/supplemental/10.1103/PhysRevB.108.075426 for phonon dispersion, cohesive energy, AIMD simulation, band dispersion, and elastic and piezoelectric properties.

[76] H. Mei, Y. Zhong, D. He, X. Du, C. Li, and N. Cheng, Predicting the structural, elastic and electronic properties of new two-dimensional carbon and silicon monolayers, Results Phys. **16**, 102826 (2020).

[77] F. Ma, M. Zhou, Y. Jiao, G. Gao, Y. Gu, A. Bilic, Z. Chen, and A. Du, Single layer bismuth iodide: Computational exploration of structural, electrical, mechanical and optical properties, Sci. Rep. **5**, 17558 (2015).

[78] M. Zhong, S. Zhang, L. Huang, J. You, Z. Wei, X. Liu, and J. Li, Large-scale 2D PbI_2 monolayers: Experimental realization and their indirect band-gap related properties, Nanoscale **9**, 3736 (2017).

[79] M. Sun, U. Schwingenschlögl, M. Sun, and U. Schwingenschlögl, Structure prototype outperforming MXenes in stability and performance in metal-ion batteries: A high throughput study, Adv. Energy Mater. **11**, 2003633 (2021).

[80] Q. Cao, X. Geng, H. Wang, P. Wang, A. Liu, Y. Lan, and Q. Peng, A review of current development of graphene mechanics, Crystals **8**, 357 (2018).

[81] Q. Peng, W. Ji, and S. De, Mechanical properties of the hexagonal boron nitride monolayer: *Ab initio* study, Comput. Mater. Sci. **56**, 11 (2012).

[82] R. C. Cooper, C. Lee, C. A. Marianetti, X. Wei, J. Hone, and J. W. Kysar, Nonlinear elastic behavior of two-dimensional molybdenum disulfide, Phys. Rev. B **87**, 035423 (2013).

[83] L. Wang, A. Kutana, X. Zou, and B. I. Yakobson, Electro-mechanical anisotropy of phosphorene, Nanoscale **7**, 9746 (2015).

[84] J. W. Jiang and H. S. Park, Mechanical properties of single-layer black phosphorus, J. Phys. D: Appl. Phys. **47**, 385304 (2014).

[85] Q. Peng, X. Wen, and S. De, Mechanical stabilities of silicene, RSC Adv. **3**, 13772 (2013).

[86] H. Zhao, Strain and chirality effects on the mechanical and electronic properties of silicene and silicane under uniaxial tension, Phys. Lett. A **376**, 3546 (2012).

[87] L. Kou, C. Chen, and S. C. Smith, Phosphorene: Fabrication, properties, and applications, J. Phys. Chem. Lett. **6**, 2794 (2015).

[88] T. Yamamoto and S. Konabe, Piezoelectric coefficients of bulk 3R transition metal dichalcogenides, Jpn. J. Appl. Phys. **56**, 098002 (2017).

[89] F. Yu, Q. Lu, S. Zhang, H. Wang, X. Cheng, and X. Zhao, High-performance, high-temperature piezoelectric BiB_3O_6 crystals, J. Mater. Chem. C **3**, 329 (2014).

[90] S. Ghosh, W. Qiao, Z. Yang, S. Orrego, and P. Neelakantan, Engineering dental tissues using biomaterials with piezoelectric effect: Current progress and future perspectives, J. Funct. Biomater. **14**, 8 (2022).

[91] H. Altammar, A. Dhingra, and N. Salowitz, Damage detection using d_{15} piezoelectric sensors in a laminate beam undergoing three-point bending, Actuators **8**, 70 (2019).

[92] Z. Yang, S. Zhou, J. Zu, and D. Inman, High-performance piezoelectric energy harvesters and their applications, Joule **2**, 642 (2018).

[93] A. R. Beattie and P. T. Landsberg, One-dimensional overlap functions and their application to Auger recombination in semiconductors, Proc. R. Soc. Lond. A **258**, 486 (1960).

[94] S. Tao, X. Zhang, J. Zhu, P. He, S. A. Yang, Y. Lu, and S. H. Wei, Designing ultra-flat bands in twisted bilayer materials at large twist angles: Theory and application to two-dimensional indium selenide, J. Am. Chem. Soc. **144**, 3949 (2022).

[95] M. I. Naher and S. H. Naqib, Possible applications of Mo_2C in the orthorhombic and hexagonal phases explored via *ab-initio* investigations of elastic, bonding, optoelectronic and thermo-physical properties, Results Phys. **37**, 105505 (2022).

[96] H. Jiang, R. Pandey, C. Darrigan, and M. Rérat, First-principles study of structural, electronic and optical properties of BaF_2 in its cubic, orthorhombic and hexagonal phases, J. Phys. Condens. Matter **15**, 709 (2003).

[97] H. Jiang, R. Orlando, M. A. Blanco, and R. Pandey, First-principles study of the electronic structure of PbF_2 in the cubic, orthorhombic, and hexagonal phases, J. Phys. Condens. Matter **16**, 3081 (2004).

[98] S. Kaprzyk and S. Niziol, The electronic structure of CoMnGe with the hexagonal and orthorhombic crystal structure, J. Magn. Magn. Mater. **87**, 267 (1990).

[99] Q. An, C. Hu, G. Yu, and H. Guo, Spin-polarized quantum transport in Si dangling bond wires, Nanoscale **12**, 6079 (2020).

[100] H. Zhang, J. Yan, Z. Ye, F. Shi, J. Piao, W. Wang, X. Gao, H. Zhu, Y. Wang, Y. Liu *et al.*, Monolithic GaN optoelectronic system on a Si substrate, Appl. Phys. Lett. **121**, 181103 (2022).

[101] H. Mori, M. Sugo, T. Sasaki, M. Tachikawa, and Y. Itoh, Integrated optoelectronic devices on Si substrates, in *Conference on Optical Fiber Communication, Vol. 4 of 1994 OSA Technical Digest Series* (Optica Publishing Group, 1994), paper TuC1.